PHYSICAL REVIEW B **79**, 144307 (2009)

Lattice dynamics and molecular rotations in solid hydrogen deuteride: Inelastic neutron scattering study

D. Colognesi,[1] F. Formisano,[2] A. J. Ramirez-Cuesta,[3] and L. Ulivi[1]
[1]*Consiglio Nazionale delle Ricerche, Istituto dei Sistemi Complessi, Sezione di Firenze, via Madonna del Piano 10, 50019 Sesto Fiorentino (FI), Italy*
[2]*CNR-INFM, CRS SOFT, Rome, Italy and OGG, Grenoble, France, c/o ILL, 6 rue Jules Horowitz, B.P. 220, F-38042 Grenoble Cedex 9, France*
[3]*ISIS Facility, Rutherford Appleton Laboratory, Chilton, Didcot, Oxon OX11 0QX, United Kingdom*
(Received 1 December 2008; revised manuscript received 22 January 2009; published 28 April 2009)

In the present paper we report inelastic neutron scattering measurements on solid low-pressure hydrogen deuteride at three different temperatures (between 4.5 and 15.6 K) using the time-of-flight spectrometers BRISP at ILL (France) and TOSCA-II at ISIS, RAL (UK). The measured double-differential cross sections give access to the proton component of the HD self-inelastic structure factor. Processed BRISP data were employed to verify the applicability of the generalized Young and Koppel model to solid HD in our kinematic range and to obtain the mean-square displacement of the molecular centers of mass. In addition, a large broadening of the first two rotational peaks was observed. A reasonable result for the density of phonon states from TOSCA-II data has been obtained, although a rigorous extraction was not possible, due to the overlap among the various spectral components. The intensity loss in the extracted density of phonon states was interpreted as the effect the phonon-roton resonance in solid hydrogen deuteride. Finally the two Bose-corrected moments of the HD phonon spectrum, related to the molecular mean-square displacement and mean kinetic energy, were simulated through a path integral Monte Carlo code. The former quantity was compared to the mentioned experimental estimates.

DOI: 10.1103/PhysRevB.79.144307 PACS number(s): 63.20.Ry, 67.80.−s, 36.20.Ng, 78.70.Nx

I. INTRODUCTION

The lattice properties of quantum crystals (^{3}He, ^{4}He, H_2, D_2, etc.) have been the subject of a large number of experimental investigations and theoretical studies. However, despite the great improvement in the understanding of these quantum systems, some of their aspects are still unclear, as proved by recent neutron scattering results on ^{4}He.[1] Moreover, if the theoretical point of view is considered, the achievements in describing quantum crystals appear even less satisfactory. It is true that the static properties of these solids (e.g., mean kinetic and potential energies, lattice constants, bulk modulus, etc.) seem reasonably well described by a number of quantum simulation methods, working either at zero temperature (such as diffusion and Green's-function Monte Carlo[2]), or at $T>0$ [such as *path integral Monte Carlo* (PIMC) (Ref. 3)]. The former Monte Carlo methods make use of an approach, attributed to Fermi and Wigner, based on analogy between the Schrödinger equation in the imaginary time domain and a classical diffusion equation, while the latter method exploits the isomorphism between a quantum particle and a peculiar type of interacting classical "ring polymer." However, as far as the quantum crystal lattice dynamics is concerned (i.e., phonon dispersion curves and density of phonon states), the scenario looks rather incomplete: the well-known self-consistent phonon theory is an excellent pragmatic method to tackle these dynamic problems, but it cannot be considered sufficiently general, and it has been recently shown that its prediction on the mean kinetic energy of high-density solid ^{3}He is not accurate.[4] On the other hand, both the *path integral centroid molecular dynamics* (PICMD) (Ref. 5) and the *ring polymer molecular dynamics* (RPMD),[6] relatively new and promising techniques, surely need further development and a more rigorous theoretical validation, at least regarding the dynamical properties of quantum crystals. These two similar approaches are still based on the isomorphism between quantum systems and interacting classical ring polymers; but, differently from PIMC, they are capable of evaluating real-time correlation functions from the classical-like trajectory of the polymer centroids evolving on the Feynman-Hibbs effective potential surface. An analogous situation can be envisaged for the competitors of the cited dynamical methods, namely, the various versions of the *linearized semiclassical initial value representation* (LSC-IVR).[7] They provide a practical way for adding quantum effects to classical molecular-dynamics simulations by replacing the nonlinear boundary value problem of the semiclassical theory with an average over the initial conditions of classical trajectories.

In a new study on solid para-hydrogen,[8] an accurate determination of the density of phonon states was extracted from inelastic neutron scattering spectra and compared to the most recent PICMD calculations.[9] An overall agreement was found, but yet a number of spectral shape details were missing or misplaced in the simulated data. These results on solid para-H_2, demonstrating the power of the method, persuaded us to continue the experimental studies on the self-dynamics of solid hydrogen isotopes, exploiting the intrinsic incoherence of the neutron scattering from protons. In fact, it is generally assumed[10] that if a sample contains some protons and some other nuclei in a similar concentration, then the result will basically consist in incoherent signal from the protons only. A topic of particular relevance in this respect is the hydrogen deuteride (HD) lattice and rotational dynamics, which has never been studied through incoherent neutron scattering. Actually the only existing inelastic neutron spectra of HD (Ref. 11) have been obtained at very high momentum transfer in the so-called the neutron Compton regime, where only the single-nucleus dynamics (mainly intramolecular) is probed. HD is peculiar since it is not only a crossover molecule between H_2 and D_2, with an intermediate quantum character owing to its mass ($M_{\mathrm{HD}}=3$ amu), but, due to the noncoincidence between the molecular center of mass and center of charge, the HD intermolecular potential is far from being isotropic with respect to the former (even in the rotational ground state). Because of this fact, conspicuous rototranslational effects have been detected through the Raman spectroscopy,[12] confirming so far the validity of the theoretical model devised by Bose and Poll.[13] The use of incoherent neutron scattering allows us to corroborate these experimental findings through a more quantitative technique and to extend the optical observations to nonzero momentum-transfer values even though the present measurements are focused on a region of the neutron spectrum characterized by low energy and momentum transfers. A comprehensive and extended test of the HD scattering law would have surely needed a different type of neutron spectrometer. In other words, within the limits of our instrumentation, we could access information on the interplay between molecular rotations and lattice anharmonic phonon distribution in a quantum crystal where the decoupling approximation,[14–16] normally used for H_2 and D_2, is more critical.

The rest of the paper will be organized as follows. The experimental procedure will be described in detail in Sec. II. In Sec. III, we will work out the scattering law for hydrogen deuteride from the experimental spectra. In addition, we will obtain information both on the HD density of phonon states (using the isotropic Gaussian approximation to estimate the unwanted multiphonon contributions), and on the rotational form factors for the $j=0 \rightarrow j'=0$ and $j=0 \rightarrow j'=1$ transitions (j and j' are the initial and final rotational quantum numbers, respectively). In Sec. IV we will discuss the experimental results, and some physical quantities derived from the experimental spectra will be compared to their estimates obtained from original PIMC simulations. Section V will finally be devoted to conclusions and perspectives.

II. EXPERIMENTAL DETAILS

Neutron scattering measurements were carried out on BRISP and TOSCA-II spectrometers. BRISP (Ref. 17) is a so-called hybrid-geometry spectrometer, where a crystal-monochromator fixes the incident neutron energy (E_0) and a chopper system determines the final neutron energy (E_1) by time-of-flight analysis. The access to the low-momentum-transfer inelastic region is made possible by the combination of such an instrumental geometry with a two-dimensional small-angle detector array. The inclined thermal neutron beam emerging from the reactor is first collimated (divergence: 0.4°) before impinging, with a Bragg angle of 17.1°, on the focusing monochromator having an average mosaic spread of 0.4°. In the case of our experiment the selected value of incident energy was 49.92 meV, exploiting the (111) Bragg reflection from a copper crystal. A rotating disk chopper is generally used to minimize background neutrons from the beam and, by a proper phasing with respect to a Fermi chopper further downstream, to suppress contaminations from higher-order monochromator reflections. From the disk chopper onwards, neutrons are traveling in vacuum in order to get rid of small angle scattering from air. The long neutron pulses produced by the disk chopper travel through a 2-m-long honeycomb collimator, which causes the neutron beam to converge at the detector position. Neutrons leaving the collimator are finally reduced to short pulses by the Fermi chopper. Neutrons scattered by the sample are then collected by the multitube position-sensitive ^{3}He detector, covering a 2.1 m^2 area around the direct beam. A small-angle range between 1.0° and 13.4° can be continuously covered after fixing the sample-to-detector distance to 4.5 m. In our experiment data have been collected in the (−19–37) meV energy-transfer range with resolution $\Delta E=1.40$ meV at the elastic line. This made possible the collection of inelastic spectra in the thermal region at momentum-transfer values ($\hbar Q$) approximately ranging in the following interval: $0.2 < Q < 1.2$ $\mathrm{Å}^{-1}$ (see Fig. 1 for details).

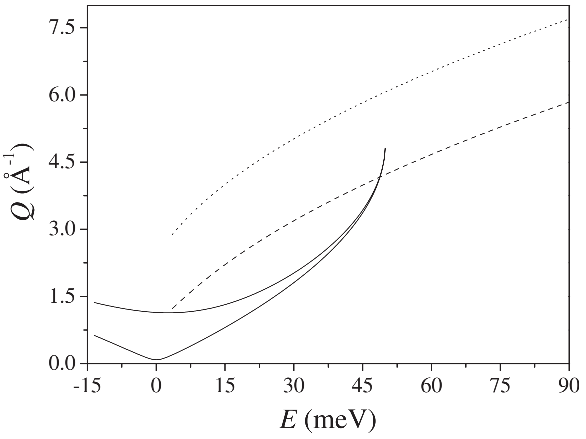

FIG. 1. Kinematic trajectories in the energy-momentum-transfer plane explored by the two neutron spectrometers employed. All the trajectories for the BRISP detectors are comprised between the two limiting curves (reported as full line), while the TOSCA trajectories are separately plotted for forwardscattering (dashed line) and backscattering (dotted line) detectors.

TOSCA-II is a crystal-analyzer inverse-geometry spectrometer operating at the ISIS pulsed neutron source (Rutherford Appleton Laboratory, Chilton, Didcot, UK).[18] The incident neutron beam spans a broad energy range, and the energy selection is carried out on the secondary neutron flight path using the (002) Bragg reflection of ten graphite single crystals, five placed in backscattering around a scattering angle of 137.7° and five in forwardscattering around a scattering angle of 42.6°. This arrangement fixes the average Bragg angles on graphite to 47.7° and 47.4° (in backscattering and forwardscattering, respectively), corresponding to scattered neutron energies of 3.32 and 3.35 meV. Higher-order Bragg reflections are filtered out by 120-mm-thick beryllium blocks, covered with cadmium and cooled down below $T=35$ K. This geometry allows to span an extended energy-transfer range even though the fixed positions of the

TABLE I. Thermodynamic conditions of the measured HD samples, including temperature *T*, pressure *p*, and molecular density *n*.

No.	T (K)	p (bar)	n (nm^{-3})
(1)	4.53(3)	0.008(6)	29.2(2)
(2)	15.61(3)	0.05(1)	28.4(2)
(3)	10.6(1)	<1.0	28.9(2)

crystal analyzers and the small values of the final neutron energy imply a variation in the momentum transfer, which is a function of the energy transfer. In this way, the two parts of TOSCA-II (namely, the backscattering and forwardscattering sections) explore two narrow stripes in the (Q, E) kinematic space, starting at $E=0$, respectively, from $Q=2.36$ and 0.92 Å^{-1}, then both increasing approximately as $(2m_nE)^{1/2}\hbar^{-1}$, where m_n is the neutron mass (see Fig. 1 for details). The resolving power of TOSCA-II is quite good $(1.5\% < \Delta E/E_0 < 3\%)$ in the energy-transfer region presently accessible by the spectrometer $(3 < E < 500$ meV).

The BRISP experimental measurements were performed at two different temperature values (namely, $T=4.53$ K and $T=15.61$ K), both at low pressure and in the hcp solid phase. A comprehensive description of the HD samples (including temperature, pressure, and molecular density) can be found in Table I. As far as the molecular density is concerned, the reported estimates were obtained from the most reliable, although scarce, thermodynamic data available in the literature.[19] After performing a background measurement of the empty orange cryostat used for the experiment, we cooled the sample container to $T=30-37$ K and we recorded its neutron spectrum. Then hydrogen deuteride (97% assay from Cambridge Isotope Laboratories) was allowed to condense in the scattering cell kept at a temperature of about 21 K. This container was made of aluminum (1.0-mm-thick walls) with a rectangular-slab geometry. The sample thickness was 1.65 mm and the internal size (i.e., 40.7×65.4 mm^2) was rather larger than the actual beam cross section (25.0×45.0 mm^2). The pressure of the gas handling system was set to $p=1.0$ bar in order to make sure that the cell was filled up with liquid [the saturated vapor pressure of 1.013 bar corresponds to $T=22.14$ (Ref. 19)]. When the cell was completely filled with liquid HD the solid sample was obtained by quickly cooling the cryostat to 5 K. This procedure guaranteed the formation of a real polycrystalline solid, which was actually checked on TOSCA-II (see below for details) by comparing spectra taken at similar values of the equatorial scattering angle θ but at completely different azimuthal angles ϕ. No differences larger than the data statistical uncertainties were ever detected. The second sample (namely, the hcp solid at $T=15.61$ K) was prepared simply by quickly heating the previous sample. This second spectrum was recorded following a procedure similar to the one outlined above. Additional measurements including a vanadium plate, a cadmium absorber, and a cadmium mask were also performed. As for the TOSCA-II measurement, operated at low pressure and $T=10.6$ K, the experimental procedure was similar to that employed on BRISP, with the only notable exception of the scattering cell: this was made of aluminum (1.0-mm-thick walls) with a circular-slab geometry. The sample thickness was 1.0 mm and the cell internal diameter (57.0 mm) was slightly larger that the TOSCA-II beam cross section (squared, 40.0×40.0 mm^2).

III. DATA ANALYSIS

The experimental time-of-flight data were transformed into energy-transfer spectra, detector by detector, making use of standard routines available on the two spectrometers including the removal of the $(E_1/E_0)^{1/2}$ kinematic factor. Then spectra were corrected for the detector efficiency or the incoming neutron flux, respectively, in the case of BRISP and TOSCA-II. At this stage data were added together following two different procedures: on BRISP, considering the polycrystalline character of the sample, 11 data blocks were produced by summing spectra recorded by detectors placed at similar θ values $(\pm 0.5°)$ but at different ϕ values. In this way we ended up with eleven fixed-angle spectra along the kinematic paths comprised between the two limiting curves (i.e., those representing data blocks 1 and 11) reported in Fig. 1. On the contrary, only two distinct data blocks were obtained for TOSCA-II: one including the backscattering detectors and the other the forwardscattering ones. This procedure was justified by the narrow angular θ range spanned by each set of detectors.[18] Thus we worked out two fixed-angle spectra along the TOSCA-II kinematic paths plotted in Fig. 1. Subsequently the empty cryostat and the sample container contributions were removed from all the HD measurements properly taking into account the sample and cell transmissions.[20] After this subtraction the important correction for the HD self-attenuation was performed. It is applied to the experimental measurements through the analytical approach suggested by Agrawal[21] in the case of a flat slablike sample: no simplified model was employed for the hydrogen deuteride total scattering cross section, which, on the contrary, was obtained from the experimental results of direct neutron measurements.[22] In addition BRISP data blocks were also normalized to the same arbitrary constant making use of the ancillary vanadium measurement performed. At this stage of the analysis, BRISP and TOSCA fixed-angle spectra, $I(E,\theta)$, appeared as in Fig. 2 and still contained four main unwanted contributions: (a) multiple-scattering events; (b) single-scattering events due to the deuterium self-dynamics; (c) single-scattering events due to the dynamic correlation between H and D in the same molecule; (d) single-scattering events due to all the dynamic correlation between atoms belonging to different molecules. The first three terms were removed after simulating them in the framework of the simple *generalized Young and Koppel* (GYK) model[14–16] for the rotational dynamics (adapted to HD), together with the isotropic Gaussian approximation[23,24] for the HD center-of-mass dynamics. The adaptation of GYK model to HD means that we have employed the same assumptions of this model for the orbital nuclear motion but not for the spin and scattering-length parts, which are influenced by the indistinguishable nature of the two nuclei in H_2 and D_2. Actually the spin and scattering-length parts of the HD-adapted GYK

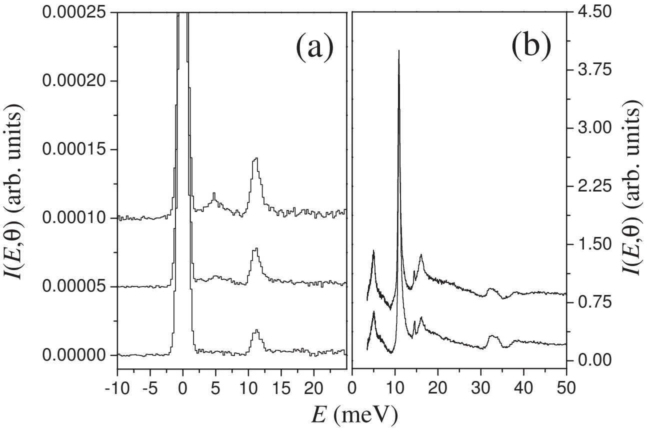

FIG. 2. Examples of solid-HD fixed-angle spectra from BRISP (a) and TOSCA-II (b) plotted as histograms. In panel (a) sample-(1) spectra (as in Table I) are reported for angles of 1.01°, 7.75°, and 13.37° (bottom to top); while in panel (b) sample-(3) spectra (as in Table I) are reported for forwardscattering and backscattering detectors (bottom to top). In both panels curves are vertically shifted for graphic reasons.

model are simple and do not differ from those of an ordinary heteronuclear diatomic molecule.[25] On the contrary the forth term was found irrelevant in the present context and neglected. Details of this kind of procedure, already successfully employed in the case of other hydrogen isotopes [i.e., solid parahydrogen,[26] solid normal deuterium, and parahydrogen impurities in D_2 (Ref. 27)] can be obtained in the literature. The three aforementioned contributions were found of modest intensity, but not negligible, both in the case of BRISP and TOSCA-II data. The rationale behind this part of the data correction and the various approximations involved is based on the fact that the incoherent neutron scattering cross section for H [$\sigma_{\rm inc}(\mathrm{H})=80.26$ b] is 2 orders of magnitude larger than its coherent counterpart [$\sigma_{\rm coh}(\mathrm{H})=1.7568$ b] and 1 order of magnitude larger than the total (coherent plus incoherent) cross section for D [$\sigma_{\rm tot}(\mathrm{D})=7.64$ b].[28] In order to provide quantitative figures for BRISP, we report the average percentage (over the single scattering from H) of double scattering and D single scattering for sample (1) in the range between −10 and 25 meV at $\theta=7.75°$: 3.4% and 9.1%, respectively. As for TOSCA-II, the average percentages of double scattering and single D scattering for sample (3) in the range between 3.5 and 50 meV in forwardscattering are about 14.4% and 5.1%, respectively. Concerning the H-D cross scattering, its absolute value came out slightly lower than the D one, but due to its "distinct" character its sign was not always positive. So in some spectral parts the two terms summed up, while in other parts they almost cancelled each other. Details about the meaning and the origin of the various neutron scattering terms in a heteronuclear diatomic molecule can be found in Ref. 29.

Once isolated the single-scattering H contribution, $I_{1,\mathrm{H}}(E,\theta)$, BRISP and TOSCA-II spectra were further analyzed following two distinct guide-lines: BRISP data, exhibiting a broader resolution (of the order of 1.4 meV) and lower Q-values (see Fig. 1), were employed to test the validity of the GYK model applied to HD, which in the low-temperature limit implies the following:

$$\Sigma_{\mathrm{H}}(E,Q) = \frac{\sigma_{\mathrm{H}}}{4\pi}\exp[-2W_{v,\mathrm{H}}(Q)] \times \sum_{j'=0} (2j'+1) j_{j'}^2(Q|\vec{r}_{\mathrm{H}}-\vec{R}|)\,\delta(E-E_{j'}) \otimes S_s(Q,E), \qquad (1)$$

where $\Sigma_{\mathrm{H}}(E,Q)$ is the generalized proton scattering law [actually proportional to $I_{1,\mathrm{H}}(E,\theta)$ once Q is taken as an appropriate function of E and θ], σ_{H} is the H total scattering cross section, $\exp[-2W_{v,\mathrm{H}}(Q)]$ is the intramolecular Debye-Waller factor[16] for H, $j_l(x)$ is the l-order spherical Bessel function, $|\vec{r}_{\mathrm{H}}-\vec{R}|$ is the distance between H and the center of mass in HD, $S_s(Q,E)$ is the center-of-mass self-inelastic structure factor, and $E_{j'}$ is the energy of the j' final rotational state. It is worth reminding that, as mentioned in the introductory section, the GYK model implies the decoupling between rotons and phonons, and its applicability to solid HD is not a consequence of its validity for (low-pressure) solid parahydrogen and normal deuterium since HD has a quite stronger anisotropic interaction. So GYK has to be experimentally tested. This has been done by fitting BRISP spectra in the $-9<E<18$ meV range (where the HD spectral features are localized) through a three-peak function obtained by summing two Gaussian profiles, $G(x,\sigma)$, and one exponentially modified Gaussian profile,[30] $M(x,\sigma,\tau)$, that is,

$$I_{1,\mathrm{H}}[E,Q(E,\theta)] = \sum_{k=1,2} A_k G(E-\epsilon_k,\sigma_k) + A_3 M(E-\epsilon_3,\sigma_3,\tau_3) + B(E), \qquad (2)$$

where A_k, ϵ_k, σ_k, and τ_k are all functions of θ, but this dependence has been dropped for brevity. The first peak, the most intense, represents the elastic line and corresponds to $j'=0$, the second, the weakest and broadest, describes approximately the HD *density of phonon states* (DoPS), and the third is the inelastic line corresponding to $j'=1$. In Eq. (2) a small linear background, $B(E)$, has been added to the fitting function. As for the other symbols employed above, $A_k(k=1,2,3)$ are the peak areas, $\epsilon_k(k=1,2,3)$ are the energy shifts, $\sigma_k(k=1,2,3)$ are the Gaussian components of the standard deviations, and τ_3 is the decay constant of the third peak. The reason to make use of $M(x)$ instead of $G(x)$ for the $j'=1$ feature will be discussed in Sec. IV. At this stage it is only important to remember that the mean value for $M(E-\epsilon_3,\sigma_3,\tau_3)$ is given by $\epsilon_3+\tau_3$, while its total standard deviation is given by $\sqrt{\sigma_3^2+\tau_3^2}$.[30] Fitted area results, A_1 and A_3, are plotted in Fig. 3 for samples (1) and (2) as a function of the Q value determined by the peak mean energy and the detector angle, while the other parameters, namely, mean and total standard deviation, are rather independent of the detector angle so that they have been averaged and reported in Table II. Parameters describing the second peak will not be discussed in this context since DoPS estimates can be better obtained from TOSCA-II.

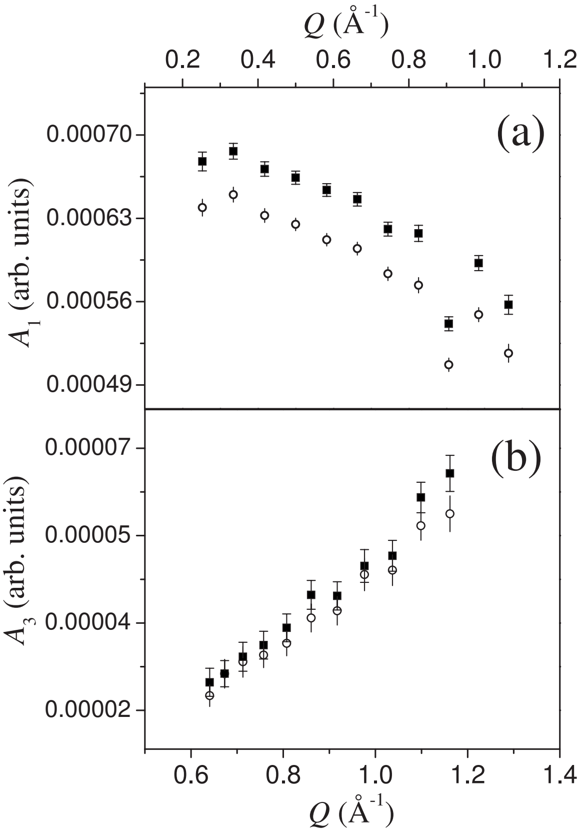

FIG. 3. Area of the rotational peaks in solid HD measured on BRISP as a function of the corresponding momentum-transfer value. Panel (a) shows A_1, the area of the elastic line (i.e., exhibiting final rotational quantum number $j'=0$), while panel (b) reports A_3, the area of the rotational inelastic peak with $j'=1$. Full squares stand for sample (1), while empty circles for sample (2), as explained in Table I.

TOSCA-II data, exhibiting a narrower energy resolution [e.g., about 0.37 meV at $E=14.42$ meV (Ref. 18) but larger Q-values (see Fig. 1), were analyzed assuming as a working hypothesis that Eq. (1) holds satisfactorily in the energy- and momentum-transfer range of interest. So the two TOSCA-II spectra, $I_{1,\mathrm{H}}(E,\theta_F)$ and $I_{1,\mathrm{H}}(E,\theta_B)$, where θ_F and θ_B are the forwardscattering and backscattering angles, respectively, are interpreted in the $3<E<30$ meV range according to the following GYK equation:

$$
\begin{aligned}
I_{1,\mathrm{H}}[E,Q(E,\theta)] = C\exp[-2W_{v,\mathrm{H}}(Q)]\sum_{j'=0}^{1}(2j'+1)j_{j'}^{2}(Qd_{\mathrm{H}})\\
\times\{\exp[-2W(Q)]\delta(E-E_{j'})\\
+S_{1,s}(Q,E-E_{j'})\\
+S_{m,s}(Q,E-E_{j'})\}\otimes R_{j'}(E), \qquad (3)
\end{aligned}
$$

TABLE II. Parameters from the fitting procedure of the BRISP data operated through Eq. (2), including: peak mean energy (namely, ϵ_1 for the elastic line and $\epsilon_3+\tau_3$ for the $j'=1$ inelastic peak), square root of the total peak variance (namely, σ_1 for the elastic line and $\sqrt{\sigma_3^2+\tau_3^2}$ for the $j'=1$ inelastic peak). Only averaged values are provided because of their independence of the detector angle.

No.	ϵ_1 (meV)	σ_1 (meV)	$\epsilon_3+\tau_3$ (meV)	$(\sigma_3^2+\tau_3^2)^{1/2}$ (meV)
(1)	0.006(1)	0.582(1)	11.38(6)	0.87(5)
(2)	0.006(1)	0.583(1)	11.36(7)	0.88(6)

where C is an instrumental sample-dependent constant (different in the case of θ_F or θ_B), $d_{\mathrm{H}}=0.6664r_0$ is the mean distance between the HD center of mass and the proton with r_0 being the HD effective internuclear separation [namely, 0.074118 mm (Ref. 16)], $\exp[-2W(Q)]$ is the center-of-mass Debye-Waller factor, $\delta(E)$ is the elastic line of the center-of-mass dynamics, $S_{1,s}(Q,E)$ is the one-phonon component of the center-of-mass self-inelastic structure factor, $S_{m,s}(Q,E)$ is the multiphonon component of the same structure factor, while $R_{j'}(E)$ describes both the experimental resolution and the rotational broadening. In practice, two replicas of $S_s(Q,E)$, one centered in the origin of the energy scale ($E_0=0$) and the other shifted to the right by the quantity E_1, are present in the TOSCA-II spectra. Unfortunately the two replicas do not exhibit exactly the same shape since the respective weighting functions $(2j'+1)j_{j'}^{2}(Qd_{\mathrm{H}})$ are not identical, and, moreover, the associated Q values, i.e., $Q(E,\theta_F)$ and $Q(E,\theta_B)$, are different, modifying both the $S_s(Q,E)$ themselves and the aforementioned weighting functions (as well as the tiny intramolecular Debye-Waller factor). In addition, as it will be made clearer in Sec. IV, the rotational broadening comes out to be rather different in the two cases $j'=0$ and $j'=1$. For all these reasons a rigorous extraction of $S_s(Q,E)$ and, from it, of $S_{1,s}(Q,E)$ does not seem to be fully achievable; however some important features of the solid-HD DoPS could be still extracted. In the rest of the data analysis we will consider only forwardscattering data since they are recorded at lower Q values, and so they are affected by smaller multiphonon components. The following step of the data reduction is to get rid of C and $\exp[-2W_{v,\mathrm{H}}(Q)]$ and to simulate and subtract the $S_{m,s}(Q,E)$ part of the spectra, ending with both the elastic line and the one-phonon component, which according to GYK read as follows:

$$
\begin{aligned}
\tilde{I}_{1,\mathrm{H}}[E,Q(E,\theta_F)] = \sum_{j'=0}^{1}(2j'+1)j_{j'}^{2}(Qd_{\mathrm{H}})[e^{-2W(Q)}\delta(E-E_{j'})\\
+S_{1,s}(Q,E-E_{j'})]\otimes R_{j'}(E). \qquad (4)
\end{aligned}
$$

To this aim we make use of independent estimates of the mean-square displacement of the HD center of mass $\langle\vec{u}^2\rangle_{\mathrm{HD}}$, and of the HD center-of-mass mean kinetic energy $\langle E_k\rangle_{\mathrm{HD}}$. From the former quantity the center-of-mass Debye-Waller factor is obtained in the framework of the isotropic pseudoharmonic approximation,[26] while both $\langle\vec{u}^2\rangle_{\mathrm{HD}}$ and $\langle E_k\rangle_{\mathrm{HD}}$ are indirectly used to simulate $S_{m,s}(Q,E)$. The method implies the construction of a preliminary model-DoPS, $\tilde{Z}_{\mathrm{HD}}(E)$, making use of the parahydrogen DoPS,[26] whose energies are properly scaled in order to simultaneously optimize the well-known sum rules for $\langle \vec{u}^2 \rangle_{\mathrm{HD}}$ and $\langle E_k \rangle_{\mathrm{HD}}$.[27] The rationale of this approach is the fact that $S_{m,s}(Q,E)$ is generally not very sensitive to the minute details of the DoPS (as shown in Fig. 4), but, on the contrary, seems dominated by its initial moments. Thus plugging $\tilde{Z}_{\mathrm{HD}}(E)$ into the following equation (isotropic Gaussian or pseudoharmonic approximation):

$$S_{m,s}(Q,E) \simeq \exp[-2W(Q)] \int_{-\infty}^{\infty} \frac{dt}{2\pi\hbar} e^{-iEt/\hbar} \left\{ \exp\left\{ \frac{\hbar^2 Q^2}{2M_{\mathrm{HD}}} \int_{-\infty}^{\infty} \frac{d\epsilon}{\epsilon} \tilde{Z}_{\mathrm{HD}}(\epsilon) \left[\cos(\epsilon t/\hbar) \coth\left(\frac{\epsilon}{2k_{\mathrm{B}}T} \right) + i \sin(\epsilon t/\hbar) \right] \right\} - 1 \right.$$
$$\left. - \frac{\hbar^2 Q^2}{2M_{\mathrm{HD}}} \int_{-\infty}^{\infty} \frac{d\epsilon'}{\epsilon'} \tilde{Z}_{\mathrm{HD}}(\epsilon') \left[\cos(\epsilon' t/\hbar) \coth\left(\frac{\epsilon'}{2k_{\mathrm{B}}T} \right) + i \sin(\epsilon' t/\hbar) \right] \right\}, \qquad (5)$$

one obtains the desired multiphonon component. The applicability of the aforementioned approximations to quantum solids such as parahydrogen or HD is explained in details in Refs. 24, 26, and 27, while $I_{1,\mathrm{H}}[E,Q(E,\theta_F)]$ and its multiphonon contributions are reported in Fig. 4. At this stage it is worthwhile to remind that in a quantum crystal what has been called DoPS, $Z(E)$, is not a simple phonon number distribution per energy units but is given by a more complex expression:

$$Z(E) = \frac{1}{6N} \sum_{\mathbf{q},j}^{6N} \frac{EA(\mathbf{q},j;E)}{2\pi\hbar\omega(\mathbf{q},j)} \frac{1-\exp(-E/k_B T)}{1-\exp[-\hbar\omega(\mathbf{q},j)/k_B T]}, \qquad (6)$$

where $\mathbf{q}$ is a phonon wave vector contained in the first Brillouin zone of the crystal, N the number of wave vectors there, j labels the six phonon branches of an hcp lattice, $\omega(\mathbf{q},j)$ is the phonon frequency, and $A(\mathbf{q},j;E)$ is the so-called *anharmonic one-phonon response function*. Equation (6) coincides with the usual DoPS in the harmonic limit as shown in Ref. 27.

IV. RESULTS AND DISCUSSION

The parameters obtained from the fitting procedure of the BRISP data operated according to Eq. (2) have been employed to study the validity of the GYK model in low-pressure solid HD. Let us start from the positions of the two peaks (namely, $j=0 \rightarrow j'=0$ and $j=0 \rightarrow j'=1$) reported in Table II. These observed figures have to be compared to the model predictions: $E_0=0$ meV and $E_1=11.06$ or 10.91 meV (using isolated molecule data[31] or infrared solid data,[32] respectively), showing a fairly good agreement. As for the asymmetric $j=0 \rightarrow j'=1$ peaks, if instead of the total means $\epsilon_3+\tau_3$, the spectral maxima are considered (placed between 10.9 and 11.1 meV), then the agreement noticeably improves. However, dealing with the peak widths, the situation appears substantially different: GYK assumes, as in Eq. (1), resolution-limited rotational lines, which, in the present experimental configuration, exhibit an average standard deviation of 0.594(8) meV (from the vanadium calibration run). This figure is almost compatible with that of the elastic line [namely, 0.582(1) meV in sample (1)] but is clearly much lower than the corresponding standard deviation of the $j=0 \rightarrow j'=1$ peak [i.e., 0.87(5) meV]. This proves the existence of an intrinsic broadening of about 0.64(7) meV, which, as we have seen in the previous section, appears to be Q independent between 0.6 and 1.2 Å^{-1}. In addition, from the TOSCA-II spectra we can derive slightly lower values for this quantity: 0.44(2) meV in forward scattering (i.e., at $Q=1.91$ Å^{-1}) and 0.39(2) meV in backscattering (i.e., at $Q=3.67$ Å^{-1}). It is worth reminding that all the mentioned broadening values are given as standard deviations. This relevant broadening of the $j=0 \rightarrow j'=1$ rotational line is not observed, for instance, in the solid para-H_2 spectrum,[27] and can be generically ascribed to a larger anisotropic interaction in HD than in para-H_2 but also to the fundamental difference of the character of this rotational excitation in the two solids. As a matter of fact, while in para-H_2 this line is due to a single molecule (localized) excitation that cannot propagate in the solid because this would imply an orthopara transition of the neighbor molecules, in HD the $j'=1$ roton is a collective excitation, which should manifest some dispersion. Our experimental broadening values have to be compared to independent determinations, either from optical spectroscopy or from computation. To our knowledge, no optical spectroscopic results are present in the literature, from which one could derive some information on the dispersion of the $j'=1$ roton. The bandwidth [full width at half maximum (FWHM), assuming a rectangular band shape] of this excitation has been estimated to be around 2 cm^{-1} (i.e., 0.25 meV).[33] A larger value, namely, 0.65 meV, is quoted in Ref. 34. A more recent calculation, which takes into account an additional term in the expansion of the intermolecular interaction potential but considers only rotons with wave vector parallel to the crystallographic c axis, gives a smaller value for this bandwidth (FWHM), namely, 1.16 cm^{-1} (i.e., 0.14 meV).[35]

Of particular interest is the line corresponding to the transition $j=0 \rightarrow j'=2$, appearing in the TOSCA-II spectra at about $E \simeq 33$ meV, which is quite intense in HD, in contrast with para-H_2, due to the contributions of the incoherent proton cross section to this molecular transition. Large standard deviations are extracted from this feature, namely, 0.91(6) meV in forward scattering and 0.95(6) meV in backscatter-

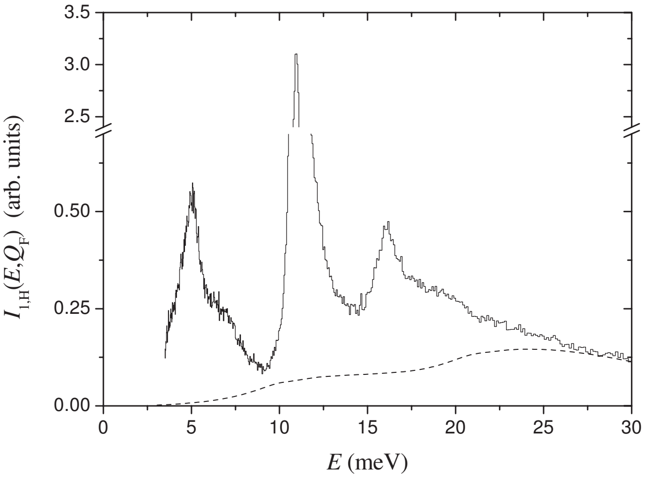

FIG. 4. Single-scattering H part, $I_{1,\mathrm{H}}[E,Q(E,\theta_F)]$, of the TOSCA-II neutron spectrum measured in forwardscattering at $T=10.6$ K (histogram), together with its simulated multiphonon component (dotted). The purely rotational transition $j=0\rightarrow j'=1$ is visible around $E=11$ meV, while two replicas of the density of phonon states show their maxima at about 5 and 16 meV, respectively.

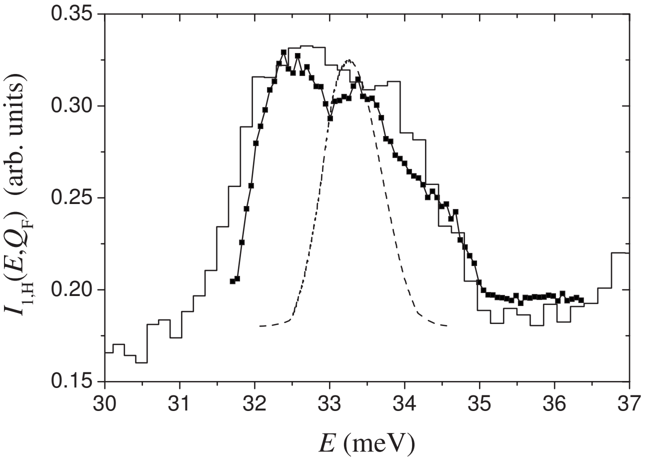

FIG. 5. Spectra of the $j=0\rightarrow j'=2$ transition in solid HD and para-H_2 obtained from different techniques: present HD neutron scattering (histogram), HD Raman scattering (Ref. 36) (dashed line), and para-H_2 Raman scattering (Ref. 40) (squares plus solid line). All the three curves have been scaled and vertically shifted for graphic reasons, while the para-H_2 one has also been horizontally shifted to account for the difference between the HD and the H_2 rotational constants.

ing, where some trace of a multiple peak structure is visible. The same transition is not easily observed in solid para-H_2 because, in this case, only the coherent neutron cross section of the proton contributes. The width and shape of this line represent the density of roton states for the $j'=2$ band. The allowed $(\mathbf{q}=0)S_0(0)$ transition in solid HD, observed by means of Raman scattering, has three components, and a FWHM of 0.764 meV.[36] Rotons at $\mathbf{q}\neq 0$ contribute, in infrared and Raman spectra, only to combination bands, which have not been observed so clearly in solid HD (Refs. 32 and 37) as in solid para-H_2.[38–40] Concerning the width of this band, our determination (i.e., FWHM$\simeq$2.77 meV) is similar to the ones found by optical spectroscopy both for HD (FWHM=2.36 and 2.51 meV, respectively, from Refs. 32 and 37) and for para-H_2 (FWHM=2.43, 2.51, and 2.15 meV from Refs. 38–40]) as shown in Fig. 5. This confirms that also in solid HD the $j'=2$ roton band is mainly broadened by the quadrupole-quadrupole interaction,[41] which is almost the same for HD as for para-H_2.

A more extensive test of the GYK model can be operated on the BRISP experimental data making use of the fitted peak intensities, $A_1(Q)$ and $A_3(Q)$ [as in Eq. (2)]. These quantities, reported in Fig. 3 for both samples (1) and (2), have to be compared to the following GYK predictions:

$$A_1(Q) = D\exp(-BQ^2)j_0^2(Qd_\mathrm{H}),$$

$$A_3(Q) = 3D\exp(-BQ^2)j_1^2(Qd_\mathrm{H}), \qquad (7)$$

where D and B, which are free parameters to be optimized, represent the overall instrumental scaling constant and the one-dimensional H mean-square displacement, respectively. The agreement between experimental data and GYK predictions is very satisfactory for both samples (exhibiting a reduced χ^2 equal to 0.91 and 0.64, respectively) and proves that the GYK model is substantially able to describe the inelastic neutron scattering from low-pressure solid HD in the present $(Q-E)$ range. The sample-(1) case is reported in Fig. 6. From the optimal value of the B parameter, if the isotropic pseudoharmonic approximation is employed, it is possible to extract an estimate of the HD center-of-mass mean-square displacement: $\langle\vec{u}^2\rangle_{\mathrm{HD}}=0.27(3)$ and 0.33(2) Å^2, respectively for samples (1) and (2). Naturally it is not enough to assess the good fit quality since it is also important to verify if these mean-square displacement estimates are realistic and sound. An analogous figure can be derived from the TOSCA-II data by comparing the areas of the $j=0\rightarrow j'$

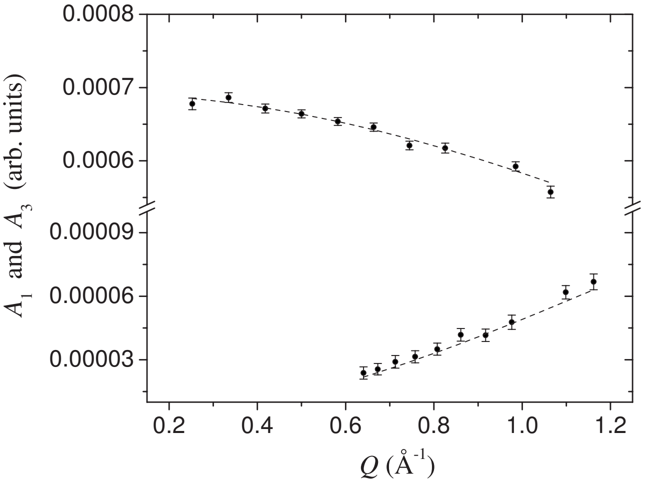

FIG. 6. Elastic (upper data) and inelastic (lower data) peak areas from solid HD at $T=4.53$ K [i.e., sample (1) in Table I] as a function of the momentum transfer. Solid dots with error bars are obtained from BRISP experimental data, while dashed line is the result of the generalized Young and Koppel model (see main text for details).

$=1$ inelastic peaks in the forwardscattering and backscattering banks. After carefully taking into account the detector efficiency (see Ref. 27 for details), the following value has been obtained for sample (3): $\langle \vec{u}^2 \rangle_{\mathrm{HD}} = 0.32(2)$ Å^2. This quantity concerns an HD sample whose density and temperature are actually in between those of samples (1) and (2), and, understandably, $\langle \vec{u}^2 \rangle_{\mathrm{HD}}$ turns out to be intermediate between the two previous estimates despite the large statistical uncertainty of all these data. Thus this last finding might be also meant as an indirect proof of the GYK validity in a wider Q range, namely, $1.91 < Q < 3.67$ Å^{-1}, even though a single point-test has a limited reliability. We will further discuss TOSCA-II data at the end of the present section.

In order to gain a better understanding of the center-of-mass mean-square displacement in solid HD, simulations are accomplished for HD at the same thermodynamic conditions of samples (2) and (3), making use of the PIMC technique. The choice of these thermodynamic conditions is motivated by the well-known advantage of doing PIMC calculation on systems at temperatures not too low if compared to their Debye temperatures. The crystallographic structure of the simulated samples is chosen according to the actual experimental situation (namely, an hcp structure with ideal $c/a = 1.633$). Among the various outputs obtainable from a PIMC simulation, mainly the radial pair-correlation function, $g(r)$, and the mean kinetic energy, $\langle E_k \rangle_{\mathrm{HD}}$, will be taken into account and discussed in the following. An *NVT* (i.e., isochoric-isothermal) PIMC code is employed, setting the molecular number density, $n = N/V$, and temperature, T, to values identical to the experimental ones. Simulations are carried out using the semiempirical isotropic pair potential derived by Silvera and Goldman,[42] and still considered one of the most reliable for hydrogen isotopes (i.e., H_2, HD, and D_2) in low-temperature condensed phases. The PIMC algorithm is accomplished by extending the number of monomers (the so-called *Trotter number*, P) of $N = 384$ ring polymers, which in the PIMC isomorphism[43] represent the quantum particles of HD, from $P = 16$ to $P = 50$. However, only small differences, mainly at short distance, are observed between these two results in the $g(r)$. Thus the $P = 16$ calculation is subsequently carried in a larger box ($N = 3072$) in order to evaluate the long-range part of the radial pair-correlation function, namely, from $r = 11$ to 22 Å, while the first part ($r \leq 11$ Å) is obtained from the slightly more accurate $P = 50$ simulation. The final PIMC result for the radial pair-correlation function is plotted at large values of r in Fig. 7 for samples (2) and (3). Another important physical quantity derived from simulations is $\langle E_k \rangle_{\mathrm{HD}}$, which turned out (after a $P \to \infty$ extrapolation) to be 66.22(4) and 67.1(1) K, respectively, for samples (2) and (3). It is worth recalling here that this code has been already successfully employed in a large number of simulations, for example, on solid H_2,[44] liquid and solid D_2,[45,46] and H_2 impurities in solid D_2.[27] The extraction of the HD mean-square displacement can be more easily obtained through a comparison of the PIMC $g(r)$ to a simple numerical uncorrelated calculation than by a direct evaluation of mean-square displacement.[47] In the uncorrelated calculation, the pair-correlation function is worked out from an ideal hcp lattice where the HD centers of mass are distributed around their equilibrium positions according to a three-dimensional isotropic Gaussian function, totally neglecting the behavior of the neighbor molecules. Assuming lattice constants identical to the PIMC ones, one ends up with a single free parameter, namely, the mean-square displacement of a molecule from its equilibrium position. Despite the great simplicity of this uncorrelated model, we expect that it becomes progressively more and more realistic as the molecule-molecule correlation decreases with the distance. Thus, neglecting, for example, the first three shells of neighbors, it is possible to estimate the value of $\langle \vec{u}^2 \rangle_{\mathrm{HD}}$ that is the one which maximizes the agreement between PIMC data and the uncorrelated model. The calculated mean-square displacement value turns out to be (after a $P \to \infty$ extrapolation): $\langle \vec{u}^2 \rangle_{\mathrm{HD}} = 0.42(3)$ and 0.38(1) Å^2, respectively, for samples (2) and (3). The quality of the agreements is clearly visible in Fig. 7, where the uncorrelated model appears able to reproduce the simulated pattern in a satisfactory way. Further details about the center-of-mass mean-square displacement evaluation can be found in Ref. 46. The agreement between the PIMC estimates of the HD mean-square displacement and the experimental ones from BRISP and TOSCA data turns out to be only fair with a discrepancy (including both the experimental and simulation uncertainties) of about 14% and 11%, respectively, for samples (2) and (3). This is clearly in contrast with our findings in the mentioned cases of solid parahydrogen and deuterium, where the two methods yielded fully compatible values of mean-square displacement. This discrepancy could be related to a possible inaccuracy of the generalized Young and Koppel model when applied to HD. In particular, as we will see later in the present discussion, one could consider that the interplay between lattice phonons and the first rotational peak affects the $\langle \vec{u}^2 \rangle_{\mathrm{HD}}$ evaluation too. However, this explanation seems more plausible in the case of TOSCA-II data, where only the $j = 0 \to j' = 1$ rotational transition is used, than in the case of BRISP, where the very intense elastic line plays an important role in the mean-

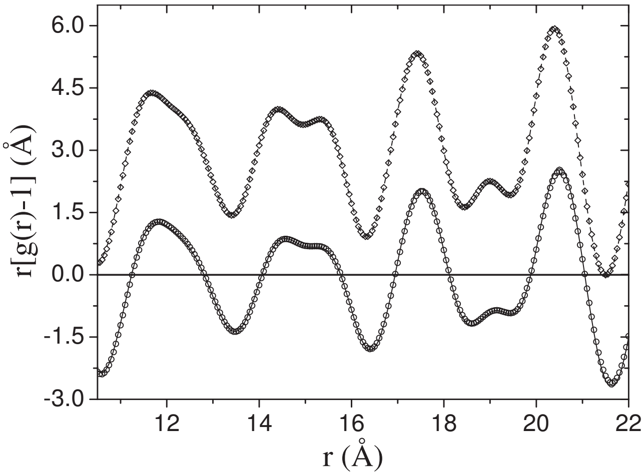

FIG. 7. Radial pair distribution functions $r[g(r)-1]$ derived from PIMC simulations (empty symbols) compared to the same quantities (lines) obtained through a simple uncorrelated lattice calculation. Circles and full line stand for solid HD at $T = 15.61$ K, while lozenges and dashed line for the same sample at $T = 10.6$ K and have been vertically shifted for graphic reasons.

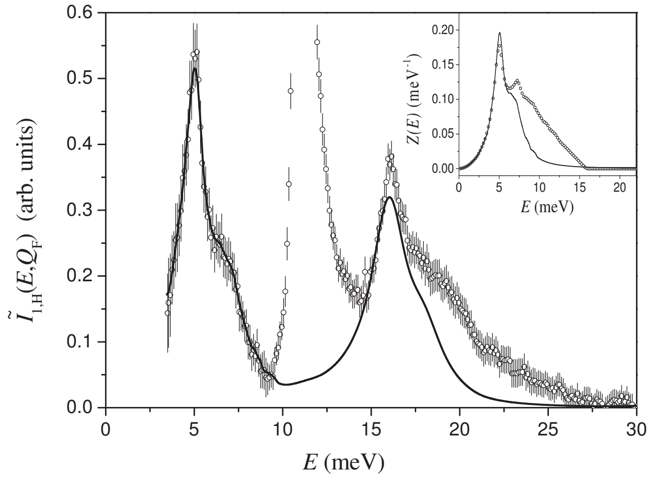

FIG. 8. One-phonon single-scattering H part, $\tilde{I}_{1,\mathrm{H}}[E,Q(E,\theta_F)]$, of the TOSCA-II neutron spectrum measured in forwardscattering at $T=10.6$ K (empty circles with error/s), together with the same spectrum (full line) reconstructed from the density of phonon states extracted from the first part of the experimental data (full line in the inset). The purely rotational line centered at about 11 meV is not included in the reconstructed spectrum. The preliminary model of density of phonon states, used to evaluated the multiphonon component, is also reported in the inset as empty circles.

square displacement determination. So at the present stage there is no fully convincing mechanism for our 11–14 % underestimation of $\langle \vec{u}^2 \rangle_{\mathrm{HD}}$.

In the last part of this section we aim to discuss the TOSCA-II results concerning the solid HD DoPS. As we have observed in Sec. III, a complete and straightforward extraction of this distribution, $Z(E)$, from the present experimental data is not possible because of the overlap among the relatively broad purely rotational transition $j=0 \rightarrow j'=1$ and the two $Z(E)$ replicas (one starting in the origin and the other shifted by the aforementioned rotational jump). However, one can try to derive a semiexperimental DoPS through this simple procedure:

(1) Constructing a DoPS through the following relationship applied to the first replica (3.5 meV$<E<$9.5 meV):

$$Z(|E|)=\exp[2W(Q)]\frac{2M_{\mathrm{HD}}}{\hbar^2 Q^2}ES_{1,s}(Q,E)[1-\exp(-E/k_{\mathrm{B}}T)], \tag{8}$$

and completing the missing parts with a Debye-like onset and a long-tail high-energy decay;[48]

(2) Evaluating the reconstructed one-phonon component of the neutron spectrum (in the framework of the usual isotropic pseudoharmonic approximation) through a combined use of Eq. (4) and the reverse of Eq. (8);

(3) Comparing this reconstructed quantity to the corresponding experimental one derived from the forwardscattering TOSCA-II data (reported in Fig. 4).

A reasonable, although still qualitative, agreement between calculated and measured spectra is obtained, and is visible in Fig. 8. Obviously the first replica is perfectly reconstructed, while the second is too narrow and not intense enough. Numerically this is not surprising, since the $Z(E)$ DoPS (also shown in Fig. 8) exhibits an area of (0.68 ± 0.04) (instead of 1.00). This is also evident by comparing $Z(E)$ to the preliminary model-DoPS, $\tilde{Z}_{\mathrm{HD}}(E)$ (used to subtract the multiphonon component), whose area was rigorously set to the unity. The two low-energy parts of the DoPSs look very similar, while $Z(E)$ decreases faster than $\tilde{Z}_{\mathrm{HD}}(E)$ after the main peak. The existence of a $(32\pm4)\%$ missing intensity in the experimental estimate of the DoPS is not at all to be ascribed to possible inaccuracies in the present data treatment; on the contrary, it is a clear experimental proof of the interplay between phonons and rotons in the HD lattice. As a matter of fact, this phenomenon has been theoretically foreseen by Zaidi[41] almost forty years ago using propagator techniques. The present scenario was clearly described by this author under the label "phonon density of states as a function of the frequency with roton resonance near the end of the Debye cutoff" (see Fig. 2 of Ref. 41). Unfortunately the use of a rather unrealistic model of DoPS (strictly of the Debye's type) makes a quantitative comparison between our findings and his predictions very difficult. However, from the aforementioned figure it is possible to verify that the qualitative behavior of the resonance between phonons and rotons is just moving intensity out of the unperturbed DoPS domain, substantially reducing its effective area. Thus the hybridization between phonon and roton states is, in our opinion, the cause of the presence of a dip in most of the spectroscopic observation, from combination bands, of the solid HD phonon band. The position of this dip, calculated from the band origin, coincides with the position of the roton excitation. In addition, the hybridization of roton states has been also observed in HD adsorbed on Vycor glass.[49] The mentioned dip appeared first in the infrared $S_0(0)$ sideband measured by Trefler *et al.*[50] and is also observed in the $Q_1(0)$ Raman sideband,[37] but it is almost absent in the $U_0(0)$ phonon sideband[51] (see Fig. 9). The last spectrum is actually quite similar to the truncated neutron-measured DoPS associated to the $j=0 \rightarrow j'=1$ transition, which hardly shows any signs of phonon-roton resonance. Phonon spectra of molecular crystals derived from optical spectroscopic data stem from the observation of spectral features due to double transitions, where a $\mathbf{q}=0$ combination of a $\mathbf{q}\neq0$-lattice phonon with a molecular excitation is observed. The phonon sideband of an allowed or forbidden intramolecular transition mimics the one-phonon density of states but often contains contributions from two (or more) phonon bands, which are weighted by suitable anharmonic coupling elements in the expansion of the potential energy in terms of the normal coordinates. In this sense a qualitative agreement of our determination of the DoPS with optical spectroscopic data should be considered more than satisfactory. In view of these considerations, the really good match of the $U_0(0)$ sideband with the DoPS might be considered fortuitous. However we believe that, in this case, the good agreement is due to the lack of other coupling mechanisms between the $j'=4$ state and the multiphonon terms.

V. CONCLUSIONS

In the present paper we have measured incoherent inelastic neutron scattering from solid low-pressure hydrogen deu-

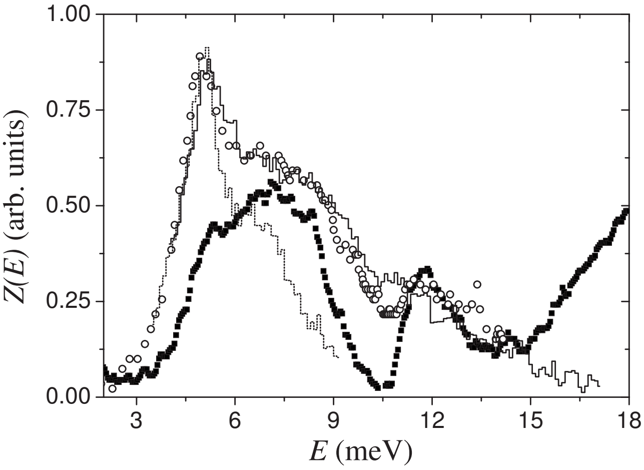

FIG. 9. Phonon spectra in solid HD obtained from different techniques: present neutron scattering in connection with the no rotational transition (dotted line histogram) and with the $j=0 \rightarrow j'=1$ rotational transition (full line histogram), Raman scattering (Ref. 37) (full squares), and infrared absorption (Ref. 51) (empty circles). All the four curves have been scaled for graphic reasons.

teride at three different temperatures (ranging between 4.5 and 15.6 K) using the time-of-flight neutron spectrometers BRISP and TOSCA-II. The measured double-differential cross sections have provided experimental access, through an elaborated data analysis, to the H contribution of the HD self-inelastic structure factor. In order to achieve this aim, measured data were corrected for the typical experimental effects (i.e., self-shielding and multiple scattering) and subtracted of the deuterium and the cross H-D unwanted signals. Subsequently BRISP spectra were used to test the applicability of the generalized Young and Koppel model to solid HD. This model has been found to be fully satisfactory in the energy-transfer–momentum-transfer range: $0 < E < 12$ meV, $0.2 < Q < 1.2$ Å^{-1}, providing, in addition, experimental estimates of the mean-square displacement of the HD centers of mass. However an exceptional intrinsic broadening of the first two rotational peaks has been verified from data from both spectrometers, quite in contrast with the elastic line, which was observed to be resolution limited. The HD mean-square displacement was also determined from the TOSCA-II spectra, where, assuming this time the generalized Young and Koppel model to hold, the contributions coming from the purely rotational dynamics were separate from those connected to the HD center-of-mass dynamics. In addition, introducing also the isotropic pseudoharmonic approximation for the low-energy TOSCA-II spectral range (i.e., $3 < E < 30$ meV), aiming to relate the HD incoherent scattering law to the density of phonon states, we were able to evaluate (and then to remove) the undesired multiphonon contribution through an accurate procedure. However, due to the overlap among various spectral components, namely, the broad purely rotational line and two replicas of the density of phonon state, a rigorous extraction of the latter distribution was not possible, differently from the cases of solid bulk parahydrogen and parahydrogen defects in solid deuterium. Nevertheless an attempt to work out a semiexperimental density of phonon states was accomplished, yielding reasonable results but also showing a relevant intensity deficit in the high frequency part. This fact was not at all unexpected and was interpreted as an effect of the phonon-roton resonance in solid hydrogen deuteride. Finally, two Bose-corrected moments of this phonon spectral function, related to important physical quantities concerning the molecular center-of-mass dynamics (namely, mean-square displacement and mean kinetic energy), were simulated through a path integral Monte Carlo code. The former quantity was compared to the aforementioned experimental estimates, representing an additional check of our detailed data analysis, but provided only a fair agreement, probably still due to the mentioned phonon-roton resonance.

ACKNOWLEDGMENTS

The excellent technical support from A. De Francesco and A. Laloni (INFM-CNR, Italy), and the scientific collaboration with U. Bafile and M. Celli (ISC-CNR, Italy) are gratefully acknowledged. This work has been financially supported by *Consiglio Nazionale delle Ricerche* (CNR, Italy) and, partially, by *Ente Cassa di Risparmio di Firenze* (under the *Firenze-Hydrolab* project) and *Regione Toscana* (under the EBH2 project).

---

[1] T. Markovich, E. Polturak, J. Bossy, and E. Farhi, Phys. Rev. Lett. **88**, 195301 (2002).

[2] D. Ceperley and M. H. Kalos, in *Monte Carlo Methods in Statistical Physics*, edited by K. Binder (Springer Verlag, Berlin, 1979).

[3] D. M. Ceperley, Rev. Mod. Phys. **67**, 279 (1995).

[4] R. Senesi, C. Andreani, D. Colognesi, A. Cunsolo, and M. Nardone, Phys. Rev. Lett. **86**, 4584 (2001).

[5] J. Cao and G. A. Voth, J. Chem. Phys. **99**, 10070 (1993).

[6] I. R. Craig and D. E. Manolopoulos, J. Chem. Phys. **121**, 3368 (2004).

[7] J. Liu and W. H. Miller, J. Chem. Phys. **128**, 144511 (2008) and references therein.

[8] D. Colognesi, M. Celli, and M. Zoppi, J. Chem. Phys. **120**, 5657 (2004).

[9] H. Saito, H. Nagao, K. Nishikawa, and K. Kinugawa, J. Chem. Phys. **119**, 953 (2003).

[10] P. C. H. Mitchell, S. F. Parker, A. J. Ramirez-Cuesta, and J. Tomkinson, *Vibrational Spectroscopy with Neutrons* (World Scientific Press, Singapore, 2005).

[11] C. A. Chatzidimitriou-Dreismann, T. Abdul-Redah, and M. Krzystyniak, Phys. Rev. B **72**, 054123 (2005).

[12] M. Ali, R. H. Tipping, and J. D. Poll, Phys. Rev. B **40**, 9863 (1989); J. J. Miller, R. L. Brooks, and J. L. Hunt, *ibid.* **47**, 14886 (1993) and references therein.

[13] S. K. Bose and J. D. Poll, Can. J. Phys. **65**, 1577 (1987).

[14] J. A. Young and J. Koppel, Phys. Rev. **135**, A603 (1964).

[15] V. F. Sears, Can. J. Phys. **44**, 1279 (1966).

[16] M. Zoppi, Physica B **183**, 235 (1993).

[17] D. Aisa, E. Babucci, F. Barocchi, A. Cunsolo, F. D'Anca, A. De Francesco, F. Formisano, T. Gahl, E. Guarini, S. Jahn, A. Laloni, H. Mutka, A. Orecchini, C. Petrillo, F. Sacchetti, J.-B. Suck, and G. Venturi, Nucl. Instrum. Methods Phys. Res. A **544**, 620 (2005).

[18] D. Colognesi, M. Celli, F. Cilloco, R. J. Newport, S. F. Parker, V. Rossi-Albertini, F. Sacchetti, J. Tomkinson, and M. Zoppi, Appl. Phys. A: Mater. Sci. Process. **74**, s64 (2002).

[19] H. M. Roder, G. E. Childs, R. D. McCarty, and P. E. Angerhofer, NBS Tech. Note **641**, 4 (1973).

[20] H. H. Paalman and C. J. Pings, J. Appl. Phys. **33**, 2635 (1962).

[21] A. K. Agrawal, Phys. Rev. A **4**, 1560 (1971).

[22] W.-D. Seiffert, Report No. EUR 4455d, Euratom (1970); W.-D. Seiffert, B. Weckermann, and R. Misenta, Z. Naturforsch. A **25A**, 967 (1970).

[23] V. F. Turchin, *Slow Neutrons* (Israel Program for Scientific Translations, Jerusalem, 1965).

[24] H. R. Glyde, J. Low Temp. Phys. **59**, 561 (1985).

[25] A. C. Zemach and R. J. Glauber, Phys. Rev. **101**, 118 (1956); A. C. Zemach and R. J. Glauber, *ibid.* **101**, 129 (1956).

[26] D. Colognesi, M. Celli, and M. Zoppi, J. Chem. Phys. **120**, 5657 (2004).

[27] D. Colognesi, M. Celli, A. J. Ramirez-Cuesta, and M. Zoppi, Phys. Rev. B **76**, 174304 (2007).

[28] V. F. Sears, Neutron News **3**, 26 (1992).

[29] S. W. Lovesey, *Theory of neutron scattering from condensed matter* (Clarendon Press, Oxford, 1984).

[30] S. B. Howerton, C. Lee, and V. L. McGuffin, Anal. Chim. Acta **478**, 99 (2003).

[31] L. Ulivi, P. De Natale, and M. Inguscio, Astrophys. J. **378**, L29 (1991).

[32] A. R. W. McKellar and M. J. Clouter, Can. J. Phys. **68**, 422 (1990).

[33] J. Van Kranendonk, *Solid Hydrogen* (Plenum Press, New York, 1983).

[34] E. Filter and W. Biem, Z. Phys. **266**, 167 (1974).

[35] M. A. Strzhemechny, Phys. Rev. B **73**, 174301 (2006).

[36] J. P. McTague, I. F. Silvera, and W. N. Hardy, in *Proceeding of the Second International Conference on Light Scattering in Solids*, edited by M. Balkanski (Flammarion, Paris, 1971), p. 456.

[37] J. J. Miller, R. L. Brooks, and J. L. Hunt, Phys. Rev. B **47**, 14886 (1993).

[38] H. P. Gush, E. J. Allin, H. L. Welsh, and W. F. J. Hare, Can. J. Phys. **38**, 176 (1960).

[39] A. Nucara, P. Calvani, S. Cunsolo, S. Lupi, and B. Ruzicka, Phys. Rev. B **47**, 2590 (1993).

[40] M. Moraldi, M. Santoro, L. Ulivi, and M. Zoppi, Phys. Rev. B **58**, 234 (1998).

[41] H. R. Zaidi, Can. J. Phys. **48**, 1539 (1970).

[42] I. F. Silvera and V. V. Goldman, J. Chem. Phys. **69**, 4209 (1978).

[43] D. Chandler and P. G. Wolynes, J. Chem. Phys. **74**, 4078 (1981).

[44] M. Neumann and M. Zoppi, Phys. Rev. A **40**, 4572 (1989).

[45] M. Zoppi and M. Neumann, Phys. Rev. B **43**, 10242 (1991).

[46] U. Bafile, F. Becherini, D. Colognesi, and M. Zoppi, Phys. Rev. B **77**, 224302 (2008).

[47] E. W. Draeger and D. M. Ceperley, Phys. Rev. B **61**, 12094 (2000).

[48] Yu. Kagan and A. P. Zhernov, Sov. Phys. JETP **20**, 1340 (1965).

[49] T. E. Huber, J. A. Perez, and C. A. Huber, Phys. Rev. B **45**, 1931 (1992).

[50] M. Trefler, A. M. Cappel, and H. P. Gush, Can. J. Phys. **47**, 2115 (1969).

[51] K. Narahari Rao, J. Mol. Struct. **113**, 175 (1984).